Supplementary Information (SI) for ChemComm.
This journal is © The Royal Society of Chemistry 2025

Supporting Information

Atomically thin boron nitride nanosheets assembled on three-dimensional NiFe-layered double hydroxide for enhanced oxygen evolution reaction

Chunbo Zhu †[a, b], Jiahui Lu †[a, c], Chenxi Wang [a, c], Mingyang Xia [a, c], Sheng Hu [a, b, c, d, *], and Yang Cao[a, b, c, d, *]

[a.] *State Key Laboratory of Physical Chemistry of Solid Surfaces, Collaborative Innovation Center of Chemistry for Energy Materials (iChEM), Xiamen University, Xiamen, 361005, China.*

[b.] *Pen-Tung Sah Institute of Micro-Nano Science and Technology, Xiamen University, Xiamen, 361005, China.*

[c.] *College of Chemistry and Chemical Engineering, Xiamen University, Xiamen, 361005, China.*

[d.] *Innovation Laboratory for Sciences and Technologies of Energy Materials of Fujian Province (IKKEM), Xiamen, 361005, China.*

[*]**Corresponding author**:

Sheng Hu (Email: sheng.hu@xmu.edu.cn)

Yang Cao (Email: yangcao@xmu.edu.cn)

†Equal contribution.

Experiment section

Materials

Acetone, isopropyl alcohol, ethylene glycol, hydrochloric acid, potassium hydroxide, sodium hydroxide, $Ni(NO_3)_2 \cdot 6H_2O$ and nitric acid were purchased from Sinopharm Chemical Reagent Co., Ltd. Boron nitride (BN) powder was purchased from Guangzhou Liangji technology Co., Ltd. The nominal particle sizes, as provided by the supplier, were 12, 22, and 50 μm. Tannic acid was purchased from Acmec. $FeCl_2 \cdot 4H_2O$ and $FeSO_4 \cdot 7H_2O$ were purchased from Macklin and Shanghai Yuanye Bio-Technology Co., Ltd, respectively. All other consumables were purchased from commercial sources and used without any purification.

Material characterizations

The surface morphology and elemental composition of the samples were characterized using a GeminiSEM 500 field emission scanning electron microscope (SEM) equipped with an energy dispersive spectrometer (EDS), operated at 5 kV. Thickness measurements of boron nitride nanosheets (BNNS) were conducted by atomic force microscopy (AFM, Cypher ES Dimension FastScan). X-ray photoelectron spectroscopy (XPS, K-Alpha, Thermo Fisher) was performed to determine their chemical compositions. X-ray diffraction (XRD, ARL EQUINOX 3500) was used to reveal the crystalline structure of the samples. Inductively coupled plasma mass spectrometry (ICP-MS, NexIon1000G) was employed to measure the BN content in the catalyst. Inductively coupled plasma optical emission spectrometry (ICP-OES, SPECTROBLUE FMX36) was used to measure loss of Ni, Fe elements after chronoamperometry (CA) test. The Zeta potential of samples' surfaces was measured using a Solid Surface Zeta Potential Analyzer (Surpass 3, Anton Paar), while the Zeta potential of the BNNS dispersion was determined using a Nano Sizer and Zeta-potential Tester (Zetasizer Nano, Malvern Panalytical).

Synthesis of ultrathin boron nitride nanosheets

Boron nitride nanosheets (BNNS) were exfoliated from BN particles (nominal size: 12 μm) via wet ball-milling method, following a reported procedure [1] with optimized parameters. The detailed procedure is described below:

The ball-milling jar and grinding balls were cleaned with deionized water and subsequently dried in an oven. Then 500 mg of BN powder was transferred to the ball-milling jar. After that, 25 g of grinding balls were added, corresponding to a ball-to-powder mass ratio of 50:1. A mixture of grinding balls with diameters of 0.5, 1.0 and 2.0 cm was used to minimize interstitial spaces and ensure efficient grinding (mass ratio of BN and TA is 5:4). Next, 400 mg of tannic acid (TA) and deionized water were added to the jar to submerge the powder and balls. The ball-milling process was then conducted at 400 rpm for 24 h. After being milled, the resulting slurry was transferred to centrifuge tubes and diluted with deionized water. The mixture was ultrasonicated for 10 minutes and then centrifuged to remove any residual TA. The resulting precipitate was collected, re-dispersed in ultrapure water, and subjected to three washing cycles involving ultrasonication and centrifugation. To isolate thinner BNNS, the dispersion was centrifuged at 5000 rpm for 10 minutes, after which the supernatant containing the thinner nanosheets was collected. This centrifugation-based size selection procedure was repeated three times to further refine the sample. The mass of the final selected BNNS divided by the initial feed mass yields the production rate.

Samples fabrication

BNNS/NiFe-LDH was fabricated through a two-step method combining electrodeposition (ED) and electrophoretic deposition (EPD).

Initially, the nickel foam (NF) substrate was cleaned by acetone and isopropanol ultrasonication for 3 minutes each, followed by deionized water rinsing. To remove surface oxides, the NF substrate was sonicated in 1 M HCl for 20 minutes. After being rinsed, it was dried in a vacuum oven for 30 minutes. Electrodeposition (ED) was conducted in a three-electrode setup and with the treated nickel foam as the working electrode, Ag/AgCl electrode as reference electrode and carbon cloth as counter electrode. In the first step, deposition was conducted in a solution containing 0.1 M $Ni(NO_3)_2 \cdot 6H_2O$, 0.003 M $FeCl_2 \cdot 4H_2O$, 0.006 M NaOH, and 0.1 mg mL^{-1} BNNS (5 mg BNNS). A constant potential of −0.2 V (vs. Ag/AgCl) was applied until a total charge density of 1 C cm^{-2} was accumulated. After each electrode was rinsed with deionized water, the second ED step was conducted in a solution of 0.1 M $Ni(NO_3)_2 \cdot 6H_2O$, 0.1 M $FeSO_4 \cdot 7H_2O$, and 0.1 mg mL^{-1} BNNS (denoted as solution ②) at the potential of −0.65 V. The ED was held at 4 C cm^{-2} to rapidly form well-structured NiFe-LDH. Given the much higher charge density required at this stage, the molar ratio of Ni/Fe in Solution ② was adjusted to 1:1, 2:1, and 3:1, as shown in Fig. S3. To note, the Ni^{2+} concentration was consistently maintained at 0.1 M. The deposition mechanism may follow chemical equation below:

$$7H_2O + NO_3^- + 8e^- \rightarrow NH_4^+ + 10OH^-$$

$$xNi^{2+} + yFe^{2+} + 2(x+y)OH^- \rightarrow Ni_xFe_y(OH)_{2(x+y)}$$

Finally, the reference electrode was removed, and a low voltage of 0.1 V was applied between the working and counter electrodes, driving BNNS to move to and adsorb on previously prepared NiFe-LDH. This electrophoretic deposition (EPD) process was continued to reach a charge density of 0.5 C cm^{-2} (in solution ②). The resulting samples were rinsed with deionized water and dried in a vacuum oven before subsequent characterization.

To note, as 0.1 mg mL^{-1} BNNS was added to the electrolyte in whole ED process of BNNS/NiFe-LDH preparation (to generate NiFe-LDH substrate), the final sample may contain a minor amount of BNNS, even though none is added during the EPD process.

For the fabrication of the pure NiFe-LDH, the same ED procedure was followed but using electrolytes that did not contain BNNS.

For the fabrication of the TA-NiFe-LDH, the same ED process was performed. For the EPD step, conditions were kept identical except that the dispersion was prepared with 4 mg of TA instead of 5 mg BNNS, corresponding to the loading ratios from BNNS exfoliation.

BNNS/NiFe-LDH on carbon paper fabrication

NiFe-LDH on carbon paper was synthesized via a hydrothermal method using a 75 mL precursor mixture of 3.6 mmol $Ni(NO_3)_2 \cdot 6H_2O$, 1.8 mmol $FeCl_2 \cdot 4H_2O$, and 0.7408 g NH_4F at 100 °C for 12 h, according to a reported procedure [1]. Then 5 mg of the resulting materials were mixed with 25 μL Nafion and 0.5 mL isopropyl alcohol by sonication. A specific volume of the ink was drop-cast dropped onto

0.5 cm × 1 cm carbon paper and dried for EPD (EPD-B solution, at 5 V and 0.2 V, to 0.5 C cm^{-2}).

Electrochemical measurements

All electrochemical measurements were performed on an electrochemical workstation, using a custom-made cell with a Hg/HgO reference electrode and a platinum counter electrode. The electrolyte was 1 M KOH solution. The measured potentials ($V_{Hg/HgO}$) were converted to reported potentials versus the reversible hydrogen electrode (RHE) using the equation (Eq. 1):

$$V_{RHE} = V_{Hg/HgO} + 0.0592 \times pH + 0.098 \quad (1)$$

Linear sweep voltammetry (LSV) curves were collected at a scan rate of 1 mV s^{-1} over a potential range from 1.3 V to 1.63 V versus RHE. All potentials were referenced to RHE with 90% iR drop compensation. Their electrochemical impedance spectroscopy (EIS) measurements were performed at the overpotential of 300 mV at a frequency ranging from 0.1 Hz to 10 kHz.

The Tafel slopes were acquired by Tafel plots from the linear portion fitting overpotential (η) versus log current density (log j) by the Tafel equation (Eq. 2), where η is the overpotential, j is the current density, and b is the Tafel slope.

$$\eta = b\ log(j) + a \quad (2)$$

To determine the electrochemical surface area (ECSA) of BNNS/NiFe-LDH, cyclic voltammetry (CV) measurements were carried out in a non-Faradaic potential window between 0.91 and 1.01 V versus RHE at various scan rates of 10, 20, 40, 60, 80, and 100 mV s^{-1}. The capacitive current was calculated as the difference between the anodic and cathodic currents at 0.96 V, $(J_{anodic} - J_{cathodic})/2$, and plotted against the scan rate. A linear trend was obtained with its slope corresponding to the double-layer capacitance C_{dl} (mF cm^{-2}). The ECSA of catalyst was estimated using Eq. 3, where C_s (0.02 mF cm^{-2}) is the specific capacitance, and A (0.2 cm^2) is the geometric surface area of the electrodes.

$$ECSA = C_{dl} \times A/C_s \quad (3)$$

During the actual electrodeposition process, deviations from the nominal Ni/Fe molar ratio may occur. The measured Ni/Fe molar ratios corresponding to the mass ratios fall within a range of approximately 0.8 to 2 (Table S7). The current densities of different samples exhibited reasonable fluctuations as shown in Fig. S6, which do not affect the overall conclusion that BNNS significantly enhances OER activity. For comparison in the main text, BNNS/NiFe-LDH and NiFe-LDH were evaluated under their respective optimal activity conditions.

In situ Raman spectra measurements

Raman spectra were acquired on a confocal microscope (Horiba LabRAM HR Evolution) with a 532 nm excitation source. The spectrometer was calibrated using a silicon wafer prior to each test. In situ electrochemical Raman measurements were conducted in a custom-designed Raman cell to monitor changes in surface species during the OER.

B and BN content calculations

Firstly, the catalyst grown on Ni foam was sonicated to detach it from the substrate, then dried and measured using a microbalance to obtain pristine mass, denoted as $\boldsymbol{m_{total}}$. Due to the chemical inertness

of BN, an acid-hydrolysis method reported in the literature [1] was used to convert them into soluble ions. The obtained powders were mixed with a certain volume of concentrated nitric acid into a Teflon-lined stainless-steel autoclave, sealed and heated at 225 °C for 14 h. The acid-hydrolysis efficiency of BN was approximately 40% [2]. The resulting hydrolyzed solution was transferred to a centrifuge tube and diluted with deionized water, reducing the acid concentration to 2% (volume of the test solution is denoted as $\boldsymbol{V}$) for the following ICP-MS analysis, and the measured concentration of B is $\boldsymbol{c_B}$. The mass of V detected by ICP-MS is $\boldsymbol{c_B} \times \boldsymbol{V}$. To account for the incomplete hydrolysis, the total B mass in the original sample is calculated as $(\boldsymbol{c_B} \times \boldsymbol{V}) / \mathbf{40\%}$. Consequently, the boron content within the catalyst is given by: $\boldsymbol{\omega(B)} = [(\boldsymbol{c} \times \boldsymbol{V}) / \mathbf{40\%}] / \boldsymbol{m_{total}}$. The calculated values are summarized in Table S1.

The mass fraction of boron nitride, $\boldsymbol{\omega(BN)}$, was calculated using the formula: $\boldsymbol{\omega(BN) = \omega(B)} \times (\mathbf{M(BN)} / \mathbf{M(B)})$, where $\boldsymbol{\omega(B)}$ is the measured mass fraction of boron, and $\mathbf{M}$ represents molar mass.

Determination of BNNS area coverage

Since the BN is loaded onto a complex three-dimensional structure, the actual surface area is calculated by the roughness factor R, where $R = C_{dl}/C_s \approx 171$ (C_{dl} is used from NiFe-LDH). Given the BN mass fraction of 3.33% and the sample mass density of 3.28 mg cm^{-2}, the BN mass density (m_ρ) is approximately 0.108 mg cm^{-2}. The density of h-BN is $\rho = 2.27$ g/cm^3, so BNNS with an average thickness of 3.2 nm has a mass density ($m_{\rho 0}$) of 'ρ * 3.2 nm' = 7.264 * 10^{-4} mg cm^{-2}.

The coverage percentage (P_{cover}) is calculated as: $P_{cover} = (m_\rho / m_{\rho 0}) / R * 100\% = 86.9\%$. Although the theoretical calculation predicts a high coverage of 86.9%, the actual visible surface area occupied by BN nanosheets (BNNS) may be lower due to their potential infiltration into porous structures during the deposition process.

Mass loss calculations

The metal mass loss reported herein refers specifically to the fraction lost via chemical dissolution into the electrolyte, not physical detachment. This is because dissolution means that active sites of the catalyst are permanently destroyed, resulting in irreversible degradation of its chemical structure. The experimental and computational procedures for determining electrode mass loss after stability testing are as follows.

The initial sample mass ($\boldsymbol{m_{total}}$) obtained in section '*B and BN content calculations*' was converted to mass per unit area ($\boldsymbol{m_s}$) by: $\boldsymbol{m_s = m_{total}/S}$, where $\boldsymbol{S}$ is the geometric area of corresponding samples. For the NiFe-LDH and BNNS/NiFe-LDH, the $\boldsymbol{m_s}$ values are about 3.09 mg cm^{-2} and 3.28 mg cm^{-2}, respectively. The pristine mass of metallic elements ($\boldsymbol{m_p}$) is determined by multiplying $\boldsymbol{m_s}$, the geometric area of the electrode (S), and the mass ratio of the metallic elements. The formula is $\boldsymbol{m_p} = \boldsymbol{m_s} \times \boldsymbol{S} \times$ (mass ratio of metallic elements). The mass ratio of metallic elements, obtained from EDS analysis, was approximately 64% in Table S5.

For the mass loss measurement of NiFe-LDH (after 30 h testing), 1 mL of the electrolyte was collected, neutralized with 63 μL of concentrated nitric acid, and then diluted for ICP-MS testing. The mass of specific dissolved metallic element is uniformly represented as $\boldsymbol{c}$, and dissolved metal mass loss was calculated as $\boldsymbol{m} = \boldsymbol{c} \times 0.05$ L × (50 mL / 1 mL), as presented in '*mass loss (mg)*' of Table S4.

For BNNS/NiFe-LDH (after 240 h testing), 10 mL of the electrolyte was collected, neutralized with 0.63 mL of concentrated nitric acid, and then analyzed by inductively coupled plasma-Optical emission spectrometry (ICP-OES). The dissolved metal mass was calculated as $\boldsymbol{m} = \boldsymbol{c} \times 0.01063$ L × (50 mL / 10

mL), presented in '*mass loss (mg)*' of Table S4.

Thus, the mass loss percentage of metallic elements was calculated as ($\boldsymbol{m}$ / $\boldsymbol{m_p}$) × 100%, shown in '*mass loss (%)*' of Table S4

O_2 production

The amount of O_2 generated was quantified using a custom-built flowmeter, connected to the anode section of an H-cell. During gas evolution, the displacement and corresponding time of a soap bubble within a calibrated glass tube was recorded. The average of several measurements was used to calculate the gas production rate, X, in mL h^{-1}. The gas yield was calculated according to Eq. 4, where P represents one standard atmospheric pressure, R is the ideal gas constant, T is the thermodynamic temperature, and S is the geometric area of the electrode.

$$\text{Gas yield} = PX / RT \times S \quad (4)$$

The Faradaic efficiency is calculated as the ratio of the experimentally measured oxygen evolution rate to its theoretical value at the applied current density. To further investigate the catalytic efficiency of the catalyst after long-term testing, we measured the oxygen production rate and Faraday efficiency during the 197th, 198th, 199th, and 200th hours, as shown in Fig. S15, which still shows a Faraday efficiency over 95%.

Explanation of active sites

In many recent studies, the active sites of NiFe-based catalysts are typically probed by testing in TMAOH.[3,4] As the tetramethylammonium ion (TMA^+) can occupy the active sites of negative oxygenated species in contact with the electrolyte. Polarization curves of BNNS/NiFe-LDH and pristine NiFe-LDH, measured in both 1 M KOH and 1 M TMAOH solutions after stabilization, are shown in the Fig. S8. Although the degree of current density suppression in TMAOH varies among the individual samples due to their inherent differences, the extent of decrease is comparable for both types of catalysts. This indicates that the primary active sites are located on the NiFe-LDH component.

This is in agreement with the in situ Raman spectroscopy data: BNNS/NiFe-LDH exhibits Ni species transformation and active oxygen species production at a lower applied potential aligned with the reduced overpotential observed in LSV curves, indicating that the formation of active oxygen species of NiFe-LDH is accelerated and is key to the enhanced activity.

The NiFe-LDH prepared on nickel foam possesses a high specific surface area and a three-dimensional porous structure. The BNNS sheets covering the material surface form a discontinuous layer and cannot fully seal the smaller internal pores. Consequently, the electrolyte can penetrate through gaps between BNNS sheets to contact and react with the active sites of the underlying NiFe-LDH. Therefore, most of the active surface of the BNNS/NiFe-LDH composite remains accessible to the electrolyte.

The stability of this structure can be explained within the same model: the overall network-like coverage by BNNS over the three-dimensional framework, together with the electrostatic interaction between BNNS and NiFe-LDH, helps maintain structural integrity during operation, thereby contributing to the observed enhancement in stability.

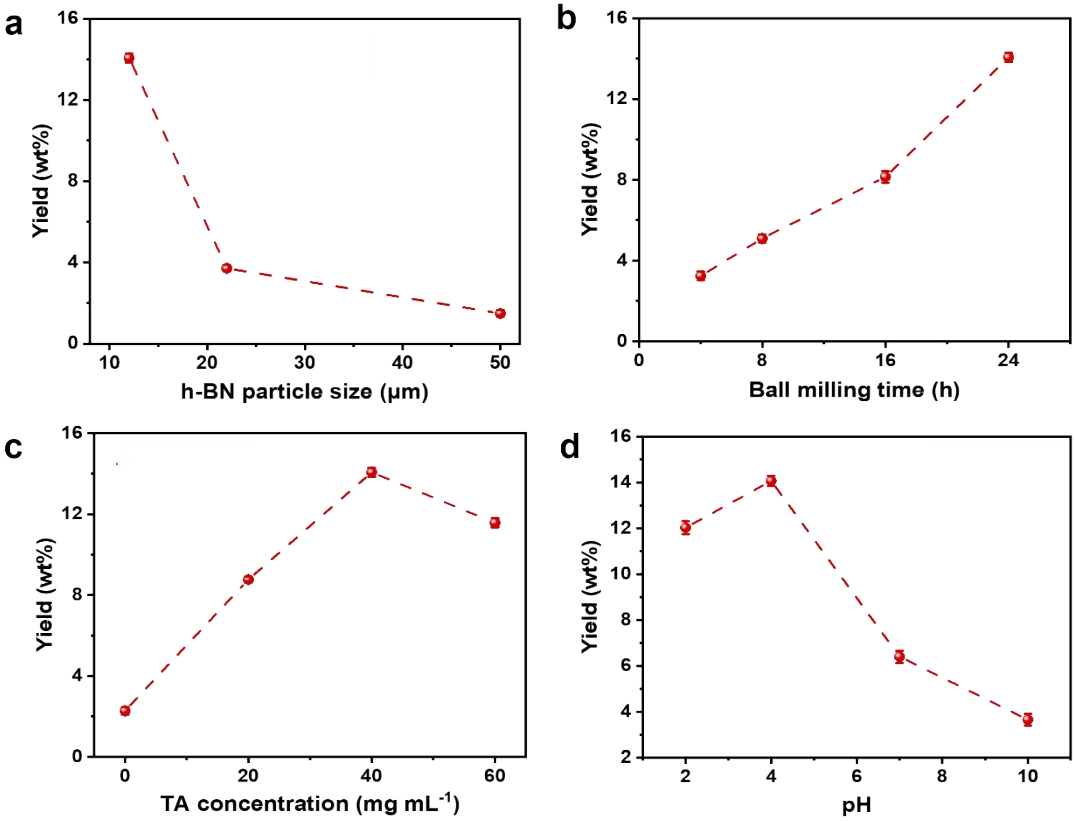

Fig. S1 Parameters of exfoliation adjustment: Relationship between (a) nominal particle size, (b) ball milling time, (c) TA concentration, (d) pH and BNNS yield (The yield is calculated as the ratio of the mass of exfoliated BNNS having a thickness less than 5 nm to the mass of the initial raw BN powder). Using 12 μm sized raw h-BN particles, TA concentration of 40 mg mL^{-1} at pH 4 and ball milling time is set to be 24 hours, we achieve a maximum yield of 14wt%.

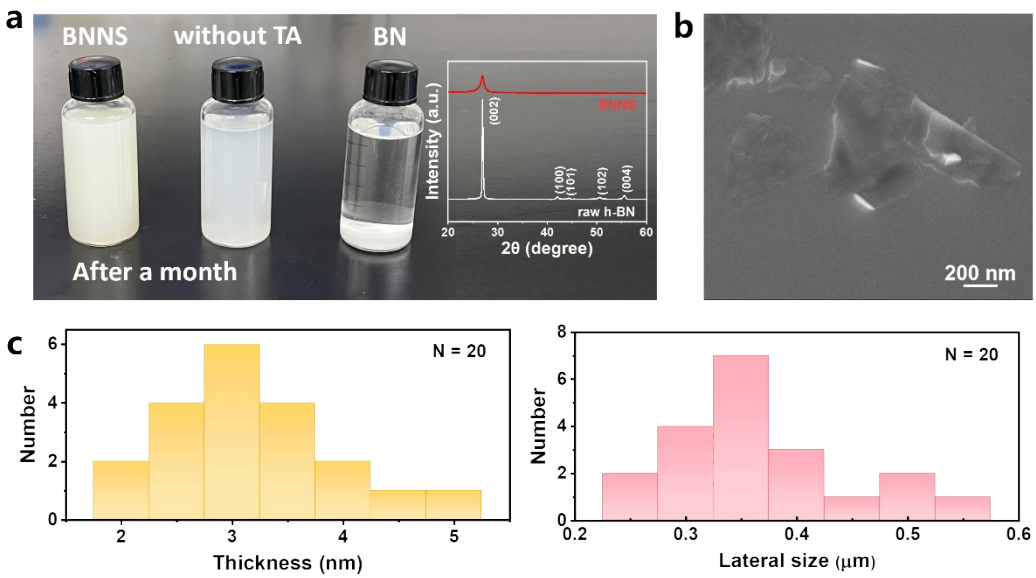

Fig. S2 (a) BNNS dispersions of TA ball-milled, non-TA ball-milled and raw h-BN (after a month). Inset: XRD characterization of BNNS and h-BN. BNNS show a highest intensity peak at a 2θ value of 26.9°, corresponding to the (002) plane. Compared to raw h-BN, peaks with reduced intensity corresponding to the (100), (101), (102), and (004) planes indicate enhanced interplanar distance, verifying synthesis of ultrathin BNNS [5, 6]; (b) SEM characterization of BNNS, scale bar: 200 nm; (c) Statistical analysis (N=20) of flake size and thickness distribution based on AFM characterization. The average thickness is about 3.2 nm (roughly ten atomic monolayers) and average lateral size is about 368 nm.

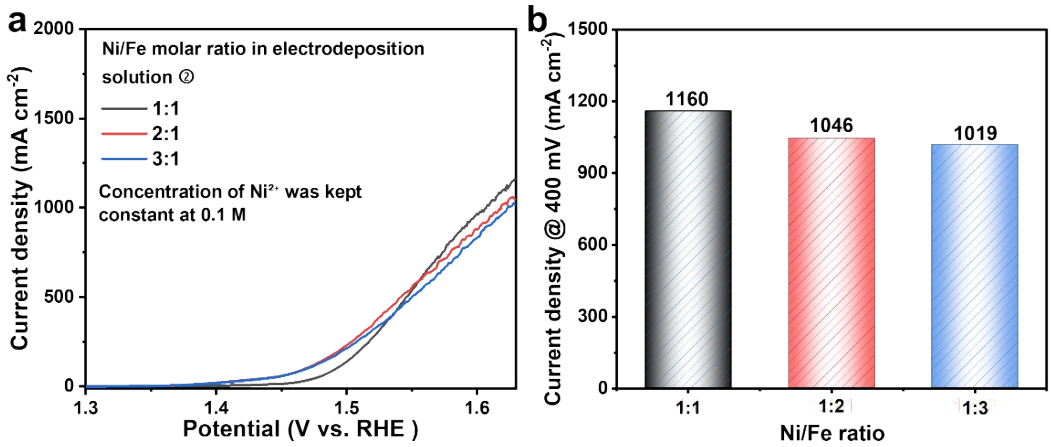

Fig. S3 (a) LSV curves and (b) current densities at 400 mV overpotential of NiFe-LDH samples prepared after whole electrodeposition process with the Ni/Fe feed molar ratio of electrodeposition solution ② tuned (the Ni^{2+} concentration was consistently maintained at 0.1 M).

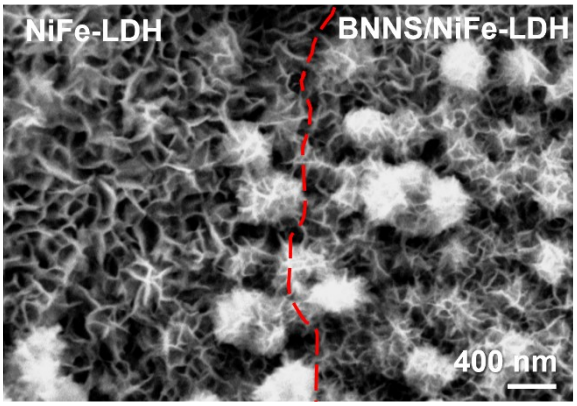

Fig. S4 SEM image of another sample showing morphological comparison of BNNS/NiFe-LDH and NiFe-LDH, demonstrating good reproducibility.

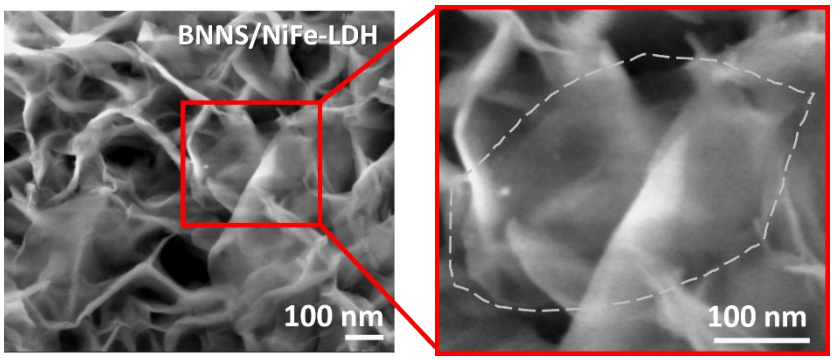

Fig. S5 High-resolution SEM images of BNNS observed on another BNNS/NiFe-LDH sample, demonstrating that the assembly of BNNS is reproducible.

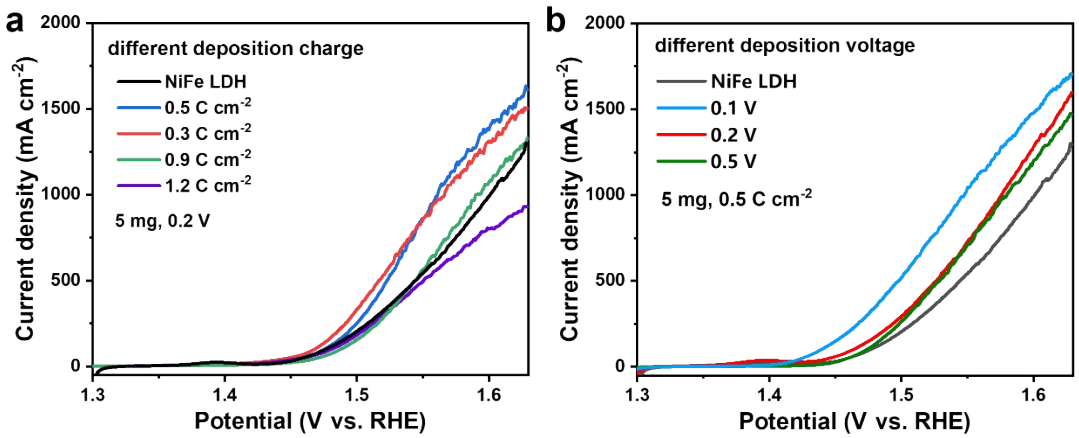

Fig. S6 OER LSV curves of samples prepared in different conditions including (a) deposition charge, (b) deposition voltage of EPD process.

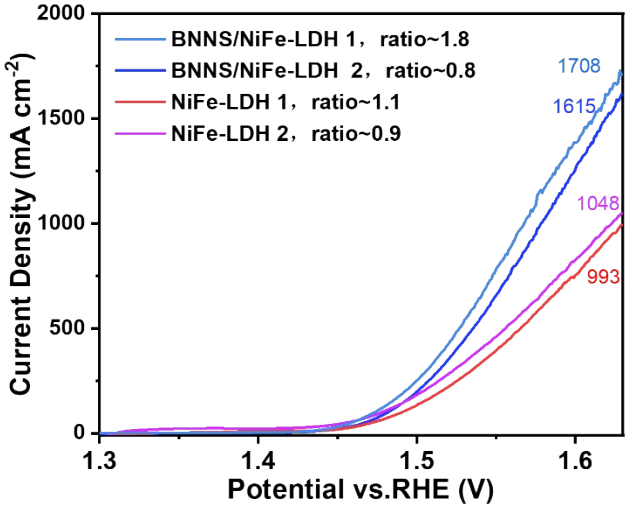

Fig. S7 LSV curves of different samples of BNNS/NiFe-LDH and NiFe-LDH with different NiFe molar ratios, showing BNNS enhanced OER activity greatly.

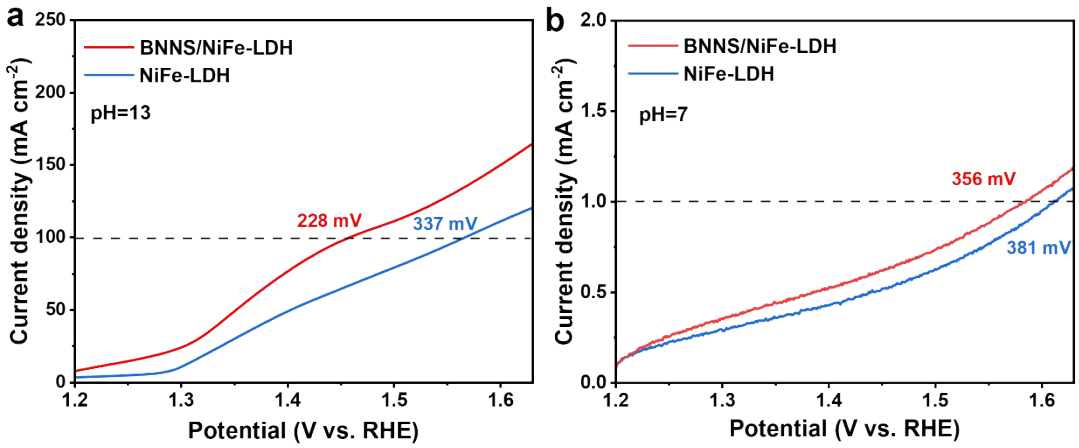

Fig. S8 LSV curves of BNNS/NiFe-LDH and NiFe-LDH at pH 13 and pH 7.

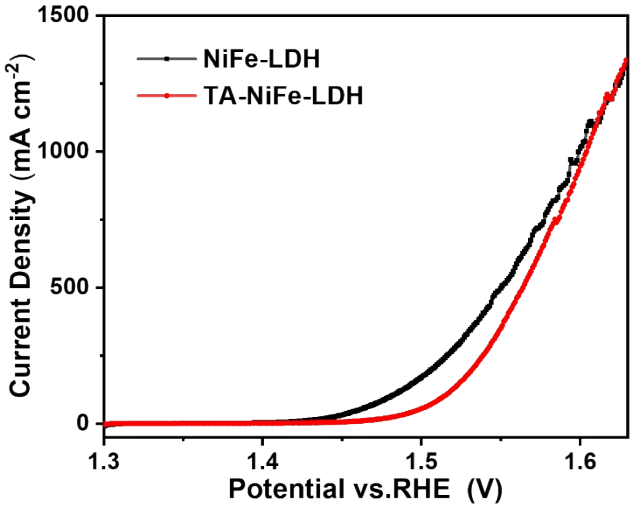

Fig. S9 OER performances of TA-NiFe-LDH and NiFe-LDH. TA-NiFe-LDH refers to a control sample deposited under identical EPD parameters from a solution that contains an equivalent mass of TA instead of BNNS, corresponding to the 5 mg feed mass of BNNS used in the composite.

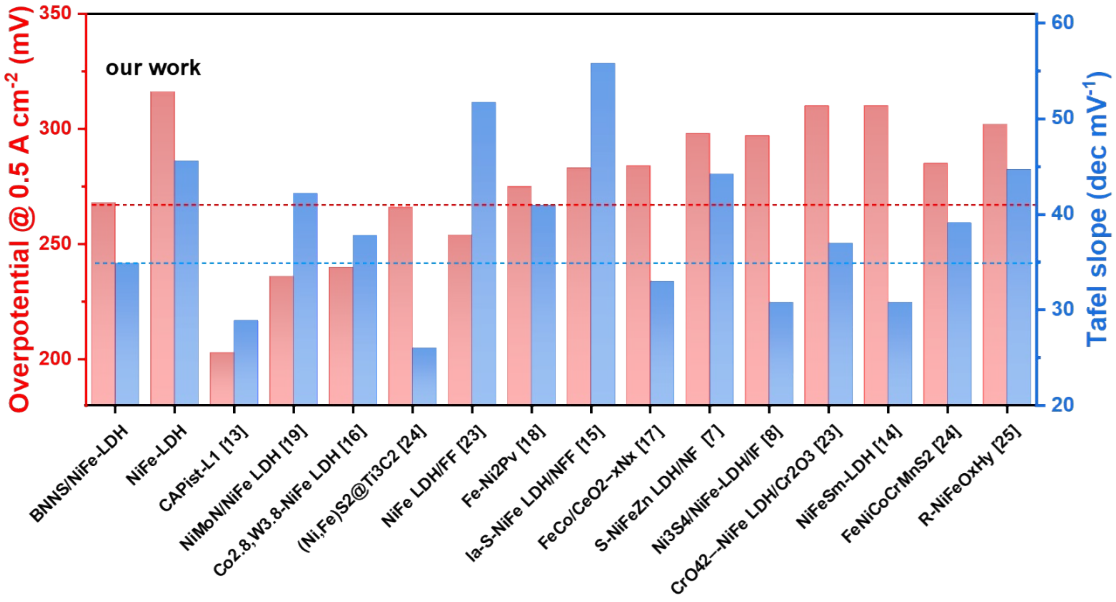

Fig. S10 Overpotential (at 0.5 A cm^{-2} current density), Tafel slope compared with other NiFe-based OER catalysts previously reported in 1 M KOH electrolytes.

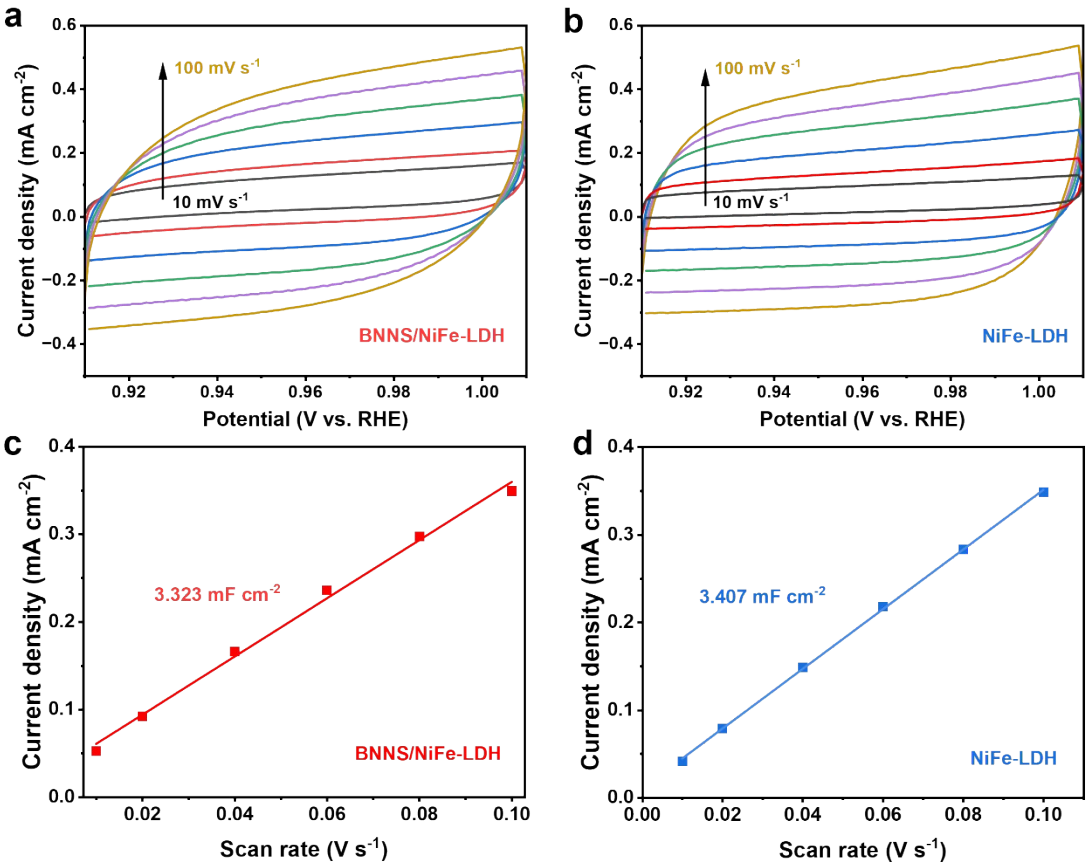

Fig. S11 The non-Faradaic (0.91 V~1.01 V) CV curves (scan rate:10, 20, 40, 60, 80,100 mV s^{-1}) and double-layer capacitance (C_{dl}) of BNNS/NiFe-LDH (3.323 mF cm^{-2}) and NiFe-LDH (3.407 mF cm^{-2}).

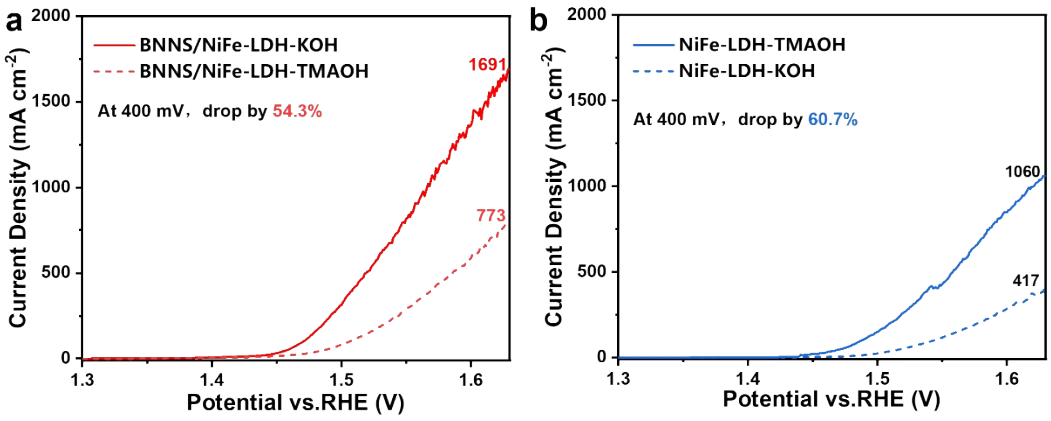

Fig. S12 LSV curves of (a) BNNS/NiFe-LDH and (b) NiFe-LDH in 1 M KOH and 1 M TMAOH. The current densities of BNNS/NiFe-LDH NiFe-LDH at 400 mV overpotential decreased by 54.3% and 60.7%, respectively.

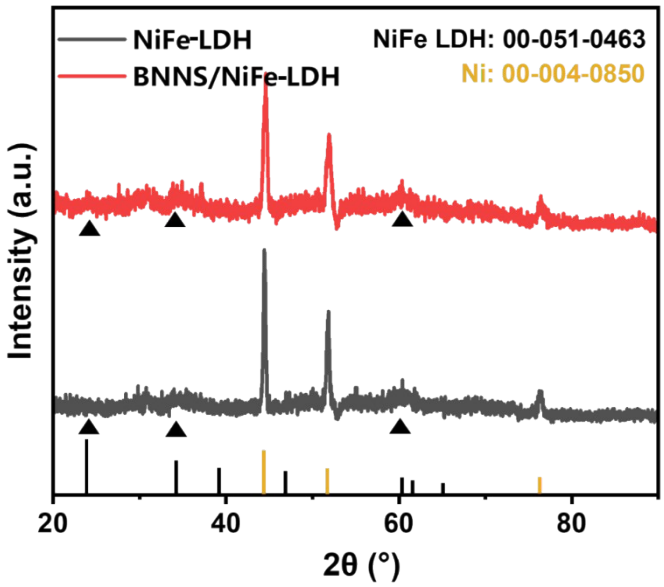

Fig. S13 XRD characterization of BNNS/NiFe-LDH and /NiFe-LDH. As synthesized catalysts show typical diffraction peaks of NiFe-LDH (JCPDS 00–051–0463). The observed Ni peaks (JCPDS 00-004-0850) arise from the Ni foam substrate. The diffraction peaks indicated with black triangles at 23.2°, 34.5°, and 60.2° are assigned to the (006), (012), and (110) planes, respectively.

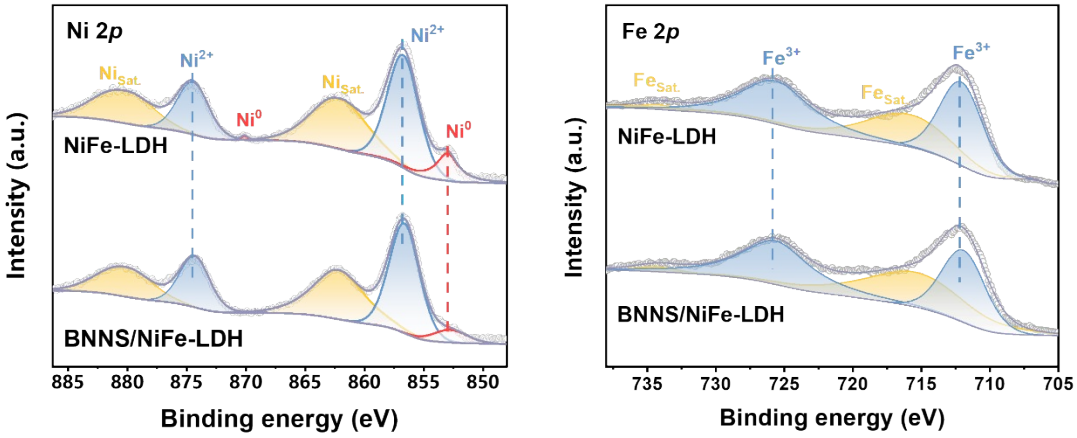

Fig. S14 XPS characterization of Ni 2p and Fe 2p spectra of BNNS/NiFe-LDH and NiFe-LDH before OER. There are negligible shifts in the peaks corresponding to the metal oxidation state between the two electrodes. The emergence of Ni^0 may generate from Ni foam.

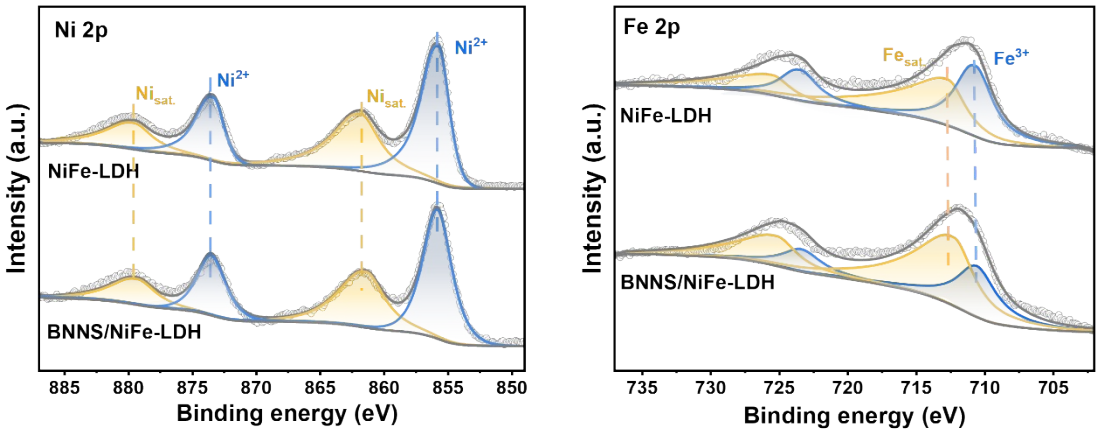

Fig. S15 XPS characterization of Ni 2p and Fe 2p spectra of BNNS/NiFe-LDH and NiFe-LDH after OER (samples were rinsed by ultrapure water and dried). Negligible shifts in the peaks corresponding to the metal oxidation state between the two electrodes. Additionally, compared with samples before OER, binding energy position of XPS spectra (without peak fitting) remains nearly unchanged.

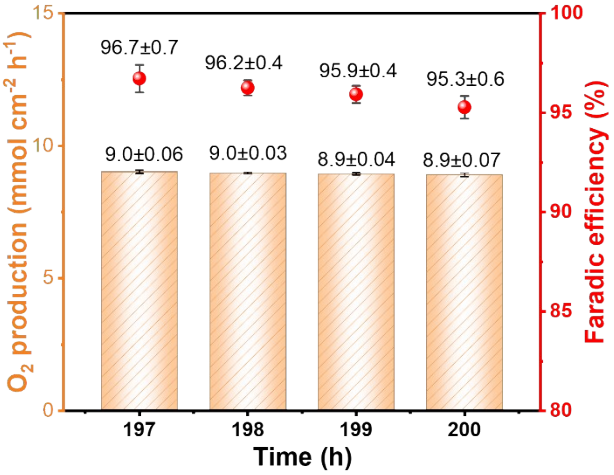

Fig. S16 The O_2 production rate and Faraday efficiency of BNNS/NiFe-LDH during the 197th, 198th, 199th, and 200th hours.

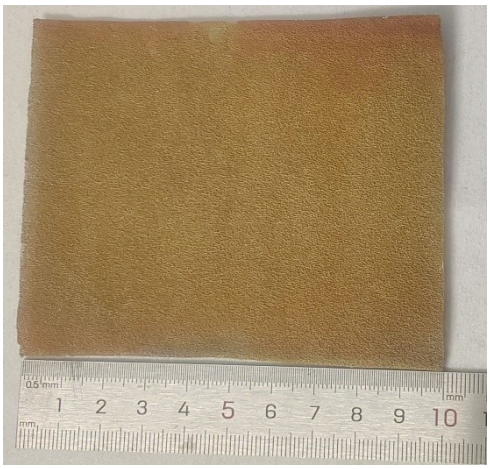

Fig. S17 Photo of 8 cm × 10 cm large-size BNNS/NiFe-LDH.

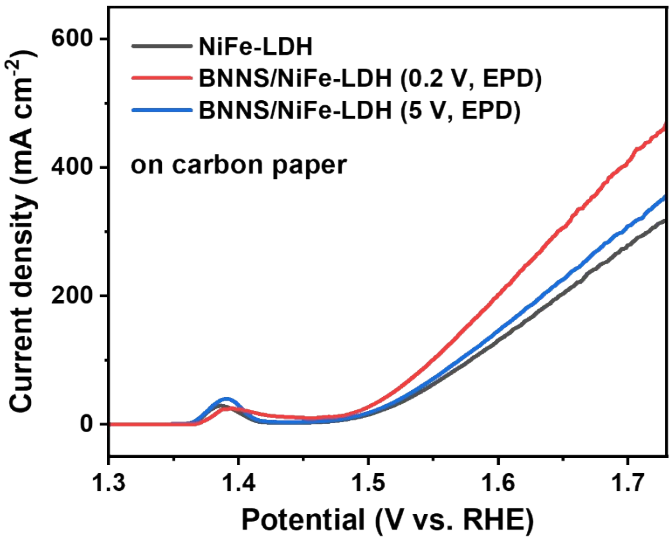

Fig. S18 LSV curves of BNNS/NiFe-LDH and NiFe-LDH (NiFe-LDH in two samples are synthesized via hydrothermal method and drop-casted on carbon paper), showing BNNS enhance the OER activity. BNNS are deposited at 5 V and 0.2 V to 0.5 C cm^{-2} in EPD process. The hydrothermal method is based on reference [2].

Table S1 B elemental content in the BNNS/NiFe-LDH with different BN feeding masses during EPD process. Here, 'Concentration' is the B concentration determined by ICP-MS, and values of 'B mass' and 'B content' are calculated according to measured values.

Feed mass	Concentration (μg L^{-1})	B mass (μg)	Sample mass (mg)	B content/%
Without BN	81	1.215	5.2	0.06
1 mg BN	297	4.455	4.8	0.23
5 mg BN	2045	30.675	5.3	1.45
10 mg BN	3785	56.775	5.05	2.81

Table S2 Comparisons of overpotentials at different representative current densities, durability and Tafel slopes for BNNS/NiFe-LDH electrode with previously reported NiFe-based OER catalysts in 1 M KOH electrolytes.

Catalysts	Scan rate (mV/s)	Overpotential (mV)			durability	Tafel slope (mV dec^{-1})	iR compen-sation
		100 mA cm^{-2}	500 mA cm^{-2}	1000 mA cm^{-2}			
BNNS/NiFe-LDH (our work)	**1**	**210**	**268**	**320**	**1 A cm^{-2}, 240 h**	**34.9**	**90%**
NiFe-LDH (our work)	**1**	**262**	**316**	**377**	**1 A cm^{-2}, 35 h**	**45.6**	**90%**
S-NiFeZn LDH/NF [7]	1	235	298	\	0.1 A cm^{-2}，400 h, remains 97.0%	44.2	95%
Ni_3S_4/NiFe-LDH/IF [8]	5	\	297	\	0.5 A cm^{-2}, 100 h, remains 96.5%	30.8	85%
CoFeP@NiFe LDH [9]	2	268	374	\	0.1 A cm^{-2}, 100 h	104	90%
NiFe-LDH-PTA [10]	2	220±3	291	342±9	1 A cm^{-2}, 500 h,	83.28	NA
Ir_{SA}-NiFe LDH/NiMo [11]	2	\	350	450	0.5 A cm^{-2}, 500 h	24	95%
NiFe-S-TCNQ [12]	5	≈268	\	\	0.1 A cm^{-2}, 2200 h	36.1	90%
NiFe LDH [13]	5	315	\	\	1 A cm^{-2}, 30 h, decrease by 25%	43.9	90%
CAPist-L1 [13]	5	\	203	220	15200 h	28.9	90%
NiFeSm-LDH [14]	2	\	310	350	0.3 mA cm^{-2}, 100 h	30.8	NA
la-S-NiFe LDH/NFF [15]	10	245	283	310	0.1mA cm^{-2}, 100 h	55.8	100%
$Co_{2.8}$, $W_{3.8}$-NiFe LDH [16]	5	\	240	255	0.5 A cm^{-2}, 200 h	37.8	95%
FeCo/$CeO_{2-x}N_x$ [17]	1	\	284	297	2 A cm^{-2}, 1000 h	33	100%
Fe-Ni_2Pv [18]	10	180	275	306	0.1 mA cm^{-2}, 100 h	41	100%
NiMON/NiFe LDH [19]	2	200	236	266	1A cm^{-2}, 250 h	42.2	85%
$NiFeO_xH_y$/hBN [20]	1	279	≈350	≈400	2 A cm^{-2}, 150 h	30	80%
MoNiFe(O)OH [21]	5	290	\	\	10 mA cm^{-2}, 70 h	23	NA
SU-NiFe-LDH(TA) @cp [22]	5	248	\	\	0.2 A cm^{-2}, 150 h	31.1	90%
NiFe LDH/FF [23]	5	216	254	362	0.5 A cm^{-2}, 100 h	51.7	95%
(Ni, Fe)S_2@Ti_3C_2 [24]	5	\	266	285	0.5 A cm^{-2}, 1000 h	26	85%
$FeNiCoCrMnS_2$ [25]	1	246	285	308	0.5 A cm^{-2}, 53 h	39.1	80%
R-$NiFeO_xH_y$ [26]	5	266	302	313	0.5 A cm^{-2}, 500 h	44.7	100%

Table S3 Dissolved Fe and Ni concentration measured by ICP-MS and ICP-OES.

Samples / Concentrations	BNNS/NiFe-LDH	NiFe-LDH
Fe (mg L^{-1})	0.0713	0.7546
Ni (mg L^{-1})	0.0269	0.1561

Table S4 Calculated values for metallic elements mass loss during EPD.

Calculated values / Samples	Mass loss (mg)		Pristine mass of total metallic elements, m_p (mg)	Mass loss (mg)	
	Fe	**Ni**		**Fe**	**Ni**
BNNS/NiFe-LDH	0.08020	0.01659	3.28 mg/cm^2*0.2 cm^2*64%=0.420	19.1	3.9
NiFe-LDH	0.17825	0.06725	3.09 mg/cm^2*0.2 cm^2*64%=0.396	45.0	17.0

Table S5 Elements content derived from EDS test.

	NiFe-LDH, sample 1,2		BNNS/NiFe-LDH, sample 1,2	
Elements	**wt%**	**wt%**	**wt%**	**wt%**
B	0.32	0.00	0.95	1.97
N	0.00	0.00	0.57	0.80
O	36.69	33.72	31.07	36.29
Ni	34.26	33.01	43.87	28.69
Fe	28.74	33.27	23.53	32.26

References

1. W. Zhu, X. Gao, Q. Li, H. Li, Y. Chao, M. Li, S. Mahurin, H. Li, H. Zhu and S. Dai, *Angew. Chem. Int. Edit.*, 2016, **55**, 10766–10770.
2. D. X. Liu, Y. Yang, J. A. Zhang, L. M. Wang, Z. W. Ma, L. Ren, J. Q. Wang, B. Xue and F. F. Li, *J. Alloy Compd.*, 2023, **941**, 168994.
3. D.Y. Chung, P. P. Lopes, P. Farinazzo Bergamo Dias Martins, H. He, T. Kawaguchi, P. Zapol, H. Y. He, D. Tripkovic, D. Strmcnik, Y. S. Zhu, S. Seifert, S. Lee, V. R. Stamenkovic and N. M. Markovic, 2020. *Nat. Energy*, 2019, **4**, 329-338.
4. Q. Jiang, S. H. Wang, C. R. Zhang, Z. Y. Sheng, H. Y. Zhang, R. H. Feng, Y. M. Ni, X. A. Tang, Y. C. Gu, Xi. H. Zhou, S. Lee, D. Zhang and F. Song, *Nat. Commun.*, 2023, **14,** 7418.
5. H. L. Fei, J. C. Dong, M. J. Arellano-Jiménez, G. L. Ye, N. D. Kim, E. L. G. Samuel, Z. W. Peng, Z. Zhu, F. Qin, J. M. Bao, M. J. Yacaman, P. M. Ajayan, D. L. Chen and J. M. Tour, *Nat. Commun.*, 2015, **6**, 10766–10770.
6. N. Wu, W. Yang, S. Che, L. Sun, H. W. Li, G. Ma, Y. K. Sun, H. C. Liu, X. B. Wang and Y. F. Li, *Compos. Part A Appl. Sci. Manuf.*, 2023, **164**, 107266.
7. F. J. Shi, L. Y. Xiao, Z. L. Zhou, X. R. Zhao, Y. Liu, J. Mao, J. Y. Qin, Y. D. Deng and J. Yang, *Adv. Funct. Mater*. 2025, **35**, 2501070.
8. Y. Liu, J. Guo, X. Liu, Z. Liu, T. Li, S. Wang, C. Zhang, K. Wang, T. Xu, W. Kong, Z. Chen, J. Huang, J. Xiao, H. Liu, H. Shao and D. Wang, *Angew. Chem. Int. Ed.*, 2025, **64**, e202516894.
9. X. Li, Y. Dong, Z. X. Dai, L. Y. Zhang, B. H. An, N. Li, Y. Q. Gao and L. Ge, *J. Colloid. Interf.* Sci., 2025, **706**, 139632.
10. J. Y. Zhang, X. F. Zhang, Z. Ma, K. Fang, L. Q. Wang, H. Ni and B. Zhao, *ACS Catal.*, 2025, **15**, 6486-6496.
11. Y. W. Wu, M. P. Chen, H. C. Sun, T. Zhou, X. Q. Chen, G. H. Na, G. Y. Qiu, D. Q. Li, N. Yang, H. S. Zheng, Y. Chen, B. X. Wang, J. H. Zhao, Y. M. Zhang, J. Zhang, F. Liu, H. Cui, T. W. He and Q. J. Liu, *Appl. Catal. B Environ.*, 2025, **360**, 124548.
12. Y. Lin, J. K. Fang, W. B. Wang, Q. L. Wen, D. J. Huang, D. F. Ding, Z. Li, Y. W. Liu, Y. Shen and T. Y. Zhai, *Adv. Energy Mater.*, 2023, **13**, 2300604.
13. Z. H. Li, G. X. Lin, L. Q. Wang, H. Lee, J. Du, T. Tang, G. H. Ding, R. Ren, W. L. Li, X. Cao, S. W. Ding, W. T. Ye, W. X. Yang and L. C. Sun, *Nat. Catal.*, 2024, **7**, 944–952.
14. M. Wang, K. S. Chen, Z. H. Yan, Y. J. Chen, H. T. Liu and X. W. Du, *Chem. Eng. J.*, 2024, **496**, 154059.
15. S. W. Song, Y. H. Wang, P. F. Tian and J. B. Zang, *J. Colloid Interf. Sci.*, 2025, **677**, 853–862.
16. Y. Shi, L. M. Song, Y. Liu, T. T. Wang, C. X. Li, J. P. Lai and L. Wang, *Adv. Energy Mater.*, 2024, **14**, 2402046.
17. S. P. Zeng, H. Shi, T. Y. Dai, Y. Liu, Z. Wen, G. F. Han, T. H. Wang, W. Zhang, X. Y. Lang, W. T. Zheng and Q. Jiang, *Nat. Commun.*, 2023, **14**, 1811.
18. X. B. Liu, Q. P. Yu, X. Y. Qu, X. P. Wang, J. Q. Chi and L. Wang, *Adv. Mater.*, 2024, **36**, 2307395.
19. P. L. Zhai, C. Wang, Y. Y. Zhao, Y. X. Zhang, J. F. Gao, L. C. Sun and J. A. Hou, *Nat. Commun.*, 2023, **14**, 1873.
20. Y. Z. Lu, B. X. Li, N. Xu, Z. H. Zhou, Y. Xiao, Y. Jiang, T. Li, S. Hu, Y. J. Gong and Y. Cao, *Nat. Commun.*, 2023, **14**, 6965.

21. Z. Y. He, J. Zhang, Z. H. Gong, H. Lei, D. Zhou, N. A. Zhang, W. J. Mai, S. J. Zhao and Y. Chen, *Nat. Commun.*, 2022, **13**, 2191.
22. X. J. Lin, Z. J. Wang, S. F. Cao, Y. Y. Hu, S. Y. Liu, X. D. Chen, H. Y. Chen, X. H. Zhang, S. X. Wei, H. Xu, Z. Cheng, Q. Hou, D. F. Sun and X. Q. Lu, *Nat. Commun.*, 2023, **14**, 6714.
23. X. H. Wei, H Xiao, Z. H. Zhang, P Han, L Wang, S. J. Deng, J. W. Wang, K Yin, H Yang, K. L. Wu and B. B. Jiang, *Small.*, 2025, **21**, e09115.
24. J. Q. Wang, Y. Liu, G. C. Yang, Y. Q. Jiao, Y. M. Dong, C. G. Tian, H. J. Yan and H. G. Fu, *Nat. Commun.*, 2025, **16**, 1319.
25. T. X. Nguyen, Y. H. Su, C. C. Lin and J. M. Ting, *Adv. Funct. Mater.*, 2021, **31**, 2106229.
26. J. Liu, W. Du, S. Y. Guo, J. Pan, J. G. Hu and X. Y. Xu, *Adv. Sci.*, 2023, **10**, 2300717.